

Electron surface scattering kernel for a plasma facing a semiconductor

F. X. Bronold and F. Willert

Institut für Physik, Universität Greifswald, 17489 Greifswald, Germany

(Dated: September 4, 2023)

Employing the invariant embedding principle for the electron backscattering function, we present a strategy for constructing an electron surface scattering kernel to be used in the boundary condition for the electron Boltzmann equation of a plasma facing a semiconducting solid. It takes the microphysics responsible for electron emission and backscattering from the interface into account. To illustrate the approach, we consider silicon and germanium, describing the interface potential by an image-step and impact ionization across the energy gap as well as scattering on phonons and ion cores by a raudium-jellium model. The emission yields deduced from the kernel agree sufficiently well with measured data, despite the simplicity of the model, to support its use in the boundary condition of the plasma's electron Boltzmann equation.

PACS numbers: 68.49.Jk, 79.20.Hx, 52.40.Hf

I. INTRODUCTION

Man-made plasmas are bounded by condensed matter. Essentially all commercially exploited technological plasmas¹ interact with either a liquid or a solid. For instance, plasmas for medical applications naturally have contact with human cells and hence with a liquid environment, whereas plasmas used for surface modification or surface catalysis are in contact with solids. Solids and plasmas are especially strongly coupled in semiconductor-based microdischarges²⁻⁴, where the surface to volume ratio is particularly large, making the interaction with the solid an integral part of the physical system. Even magnetically confined fusion plasmas interact with condensed matter in the divertor region via sheaths^{5,6} and dust particles^{7,8}, as do plasmas employed for electric propulsion in Hall thrusters^{9,10}.

Although not complete, the list indicates that a kinetic description of technological plasmas, based on equations for the electromagnetic fields and a set of Boltzmann equations for the various particle species, requires boundary conditions for the fields and the particle distribution functions. As in any Boltzmann-type modeling of kinetic phenomena¹¹⁻¹³, the latter is an integral relating at the boundary the distribution function of the outgoing particles with that of the incoming ones.

The kernel of this integral—the surface scattering kernel¹⁴—is a complicated object, because it arises from the microscopic processes at or within the bounding medium responsible for particle reflection and/or emission. Mathematical constraints enforced by the processes, such as positivity, normalization, and—in thermal equilibrium—reciprocity¹⁵, can be straightforwardly formulated, but setting up an expression for the kernel, from which quantitative data can be deduced, requires to solve the kinetic problem also partly within the bounding medium. To avoid this task, phenomenological kernels¹⁶, containing a set of adjustable parameters, are widely used. For instance, a two-term scattering kernel, describing specular and diffuse reflection, has been employed in neutron transport¹¹, gas kinetics¹², as well as plasma physics¹³.

The electron boundary condition most popular in the modeling of technological low-temperature plasmas¹⁷⁻¹⁹ even considers only specular reflection. It contains the electron reflection probability as an adjustable parameter.

Recently, however, an effort started to determine for plasma-exposed surfaces the electron reflection probability and the closely related secondary electron emission yield experimentally²⁰⁻²². The material dependence of the two parameters moves also more and more in the focus of a quantitative plasma modeling²³. It is thus appropriate to set up boundary conditions containing the wall's microphysics more faithfully than the parameterized boundary conditions used so far.

The purpose of this work is to construct a physical boundary condition for the electron Boltzmann equation of a plasma in contact with a solid. To illustrate the approach, we consider a planar semiconducting plasma-solid interface, as it occurs in semiconductor-based microdischarges²⁻⁴. Instead of resolving the electron kinetics inside the solid by a separate Boltzmann equation, we employ the invariant embedding principle²⁴⁻²⁶ to set up an integral equation for the backscattering function which is closely related to the surface scattering kernel. We employed this approach before to calculate, at low energies, the electron sticking coefficient for dielectrics²⁷ and the secondary electron emission yield²⁸ for metals. Using the backscattering function derived by one of the authors in a previous work²⁷, Cagas and coworkers²⁹ also set up a boundary condition for the electron Boltzmann equation in the manner we propose in this work. Their implementation did however not include the internal scattering cascades. Moreover, they mainly discussed numerical issues of the boundary condition, whereas we concentrate on its physics.

Based on the invariant embedding principle²⁴⁻²⁶ and a numerical strategy for its handling developed in nuclear reactor theory^{30,31}, we compute below an electron surface scattering kernel for a semiconducting interface. In its course we also remedy shortages of our previous work^{27,28,32,33}. The kernel includes impact ionization

across the band gap^{34–37} and is thus also valid for impact energies above the band gap. The electron multiplication associated with impact ionization required a renewed analysis of the normalization of the backscattering function. Thereby we realized that the normalization used so far^{27,28,32,33} cannot be correct, despite the reasonable sticking and emission coefficients it led to, because it gives in the limit of vanishing interface potential and particle-number conserving scattering processes an energy and angle independent emission yield of exactly one. Moreover, the work on metals²⁸ suggests, that scattering on the ion cores, which we initially thought not to be of importance at the low electron impact energies typical for plasma applications, has to be also included for dielectrics and semiconductors. Assuming, as for metals, the scattering on the cores to be incoherent, we employ for that purpose a radium-jellium model^{38,39}, distributing screened^{40–42} pseudopotentials^{43–45} randomly within the solid. Finally, the interface potential contains now also the image-charge effect⁴⁶, which significantly reduces the emission yield at very low impact energies. Since the emission yields we obtain for silicon and germanium are in reasonable agreement with measured^{47,48} as well as Monte Carlo simulation data⁴⁹, we consider the model employed in this work more reliable than the one used before²⁷. Using it in the surface scattering kernel should thus lead to plausible electron boundary conditions for plasmas in contact with semiconductors or dielectrics.

The remainder of the paper is organized as follows. In Sect. II, divided into three subsections, we present the formalism used for constructing a boundary condition for the electron Boltzmann equation of the plasma. First, in subsection II A, we define the surface scattering kernel in terms of the backscattering and transmission functions of the plasma-solid interface and relate the kernel to the incoming and outgoing electron energy distribution functions. Subsection II B presents our approach for computing the backscattering function from the embedding equation without approximation except the discretization of the integrals over energy and direction cosine. Finally, in subsection II C, the jellium-radium model is introduced with particular attention paid to the screening of the scattering potentials. Numerical results for the surface scattering kernel and the emission yield are presented in Sect. III before we conclude in Sect. IV. Technical details interrupting the flow of presentation are presented in two appendices.

II. FORMALISM

A. Surface scattering kernel

The quintessence of our approach is summarized in Fig. 1a. It shows an electron with energy E and direction cosine ξ impinging onto a laterally homogeneous planar interface at $z = 0$ and initiating an outgoing electron with energy E' and direction cosine ξ' . The motion

of the electrons is described by their total energy, measured with respect to the potential just outside the interface (just-outside potential), their direction cosines with respect to the outgoing normal of the interface, which also defines the z -axis of the coordinate system in real space, and an azimuth angle Φ , which due to the lateral homogeneity of the interface can be however integrated out. Hence the function $D(E, \xi)$, describing the transmission through the interface potential, and the function $B(E, \eta|E', \eta')$, encoding the scattering cascades inside the solid leading to outgoing electrons, are only functions of energy and direction cosine.

Measuring energy, length, and mass, respectively, in Rydberg energies, Bohr radii, and electron masses, and using the notation introduced in Fig. 1b, the surface scattering kernel $R(E, \xi|E', \xi')$ relating at $z = 0$ the electron energy distribution function $F^<(E, \xi)$ of the incoming electrons with the distribution function $F^>(E', \xi')$ of the outgoing ones is defined by²⁹

$$F^>(E', \xi') = \int_0^\infty dE \int_0^1 d\xi F^<(E, \xi) R(E, \xi|E', \xi') \quad (1)$$

with $E' \geq 0$ and

$$R(E, \xi|E', \xi') = R(E, \xi)\delta(E - E')\delta(\xi - \xi') + \Delta R(E, \xi|E', \xi'), \quad (2)$$

where $R(E, \xi) = 1 - D(E, \xi)$ is the probability for an electron with energy E and direction cosine ξ to be quantum-mechanically reflected by the interface potential and $\Delta R(E, \xi|E', \xi')$ is the part of the kernel accounting for the scattering cascades inside the solid producing a backscattered electron with energy $0 < E' \leq E$ and direction cosine ξ' .

The integral relation (1) holds for that part of the incoming electron energy distribution function which describes electrons with energy large enough to overcome the repulsive wall potential. Only this group of electrons hits the material interface and is not reflected by the wall potential. Since we measure energy from the potential just outside the interface, electrons of this group have positive energy. Likewise, electrons leaving the solid require a kinetic energy perpendicular to the interface larger than the electron affinity χ . Their total energy E' is thus also positive. Hence, the surface scattering kernel (2) is defined for $E, E' \geq 0$.

Since the scattering cascade encoded in $B(E, \eta|E', \eta')$ involves states far away from the extremal points of the conduction band, we do not employ effective electron masses inside the solid as we did before^{27,32,33}. Instead, we now simply take bare electron masses (also for the holes). This is of course an approximation, but overcoming it requires to account for the full band structure, including nonparabolicities as well as multi-valleys, which is beyond our present scope. It is also not obvious, to what extent band structure details affect the surface scattering kernel and the emission yield quantitatively. It is conceivable that many band structure de-

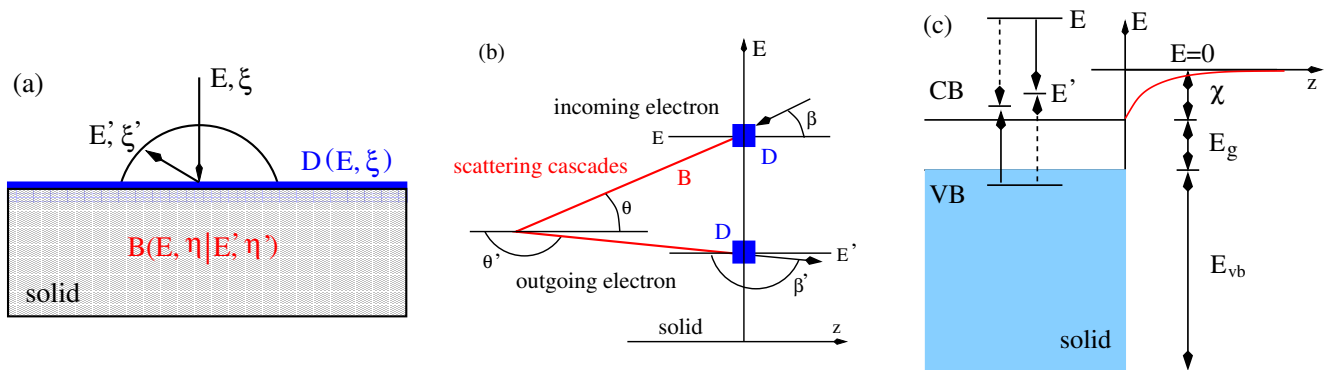


Figure 1. (Color online) (a) A primary electron with energy E (measured with respect to the just-outside potential energy) and direction cosine ξ hits a solid and leads to a secondary electron with energy E' and direction cosine ξ' . Both have to traverse the interface potential, modelled by an image-step, giving rise to the surface transmission function $D(E, \xi)$. The scattering cascades inside the solid are encoded in the backscattering function $B(E, \eta|E', \eta')$. (b) Scattering angles β, β' and θ, θ' used in the definition of the direction cosines ξ, ξ' and η, η' outside and inside the solid, respectively. (c) Two-band model used for the description of the semiconductor. The energies defining it are the electron affinity χ , the band gap E_g , and the width of the valence band E_{vb} as obtained from the density of the valence electrons. Also indicated is the image-step (in red) and an energy loss process due to direct and exchange impact ionization.

tails are washed out due to the cascade's multiple scattering. Hence, the conduction band density of states reads $\rho(E) = \sqrt{E + \chi}/2$ and the relation between the internal (η) and external direction cosines (ξ), to be obtained from the conservation of the lateral momentum and the total energy, becomes $1 - \eta^2 = (1 - \xi^2)E/(E + \chi)$ from which $\eta(\xi)$ and its inverse $\xi(\eta)$ follow. Using, $\partial\eta'/\partial\xi' = E'\xi'/((E' + \chi)\eta')$ we finally obtain³³

$$\Delta R(E, \xi|E', \xi') = \frac{E'}{E' + \chi} \frac{\xi'}{\eta'} \rho(E') \Theta(E - E') D(E, \xi) \times B(E, \eta(\xi)|E', \eta(\xi')) D(E', \xi'), \quad (3)$$

where the Heaviside step function $\Theta(E - E')$ ensures $E \geq E'$ and $B(E, \eta|E', \eta')$ is the backscattering function to which we turn in the next subsection. Before, however, we note that in terms of the surface scattering kernel, the emission yield is given by

$$Y(E, \xi) = \int_0^E dE' \int_0^1 d\xi' R(E, \xi|E', \xi'). \quad (4)$$

It can be transformed into the expression for $Y(E, \xi)$ given before^{27,28,32,33} by changing the integration variables from (E', ξ') to (E', η') and taking into account that only internal backscattered states with perpendicular kinetic energy larger than the electron affinity contribute to the emission yield.

B. Backscattering function

The central object of our approach is the backscattering function $B(E, \eta|E', \eta')$. It describes the (pseudo-)probability for an electron with energy E and direction cosine η to lead to a backscattered electron with energy

E' and direction cosine η' . In the previous work^{27,28,32,33}, we considered $B(E, \eta|E', \eta')$ as a conditional probability, obtained from the function $Q(E, \eta|E', \eta')$ normalized to the totality of all backscattered states, including those, which do not lead to electron escape from the solid. The emission yields we obtained turned out to be in good agreement with experimental data suggesting that the normalization is indeed required. However, in the course of the present investigation we realized that the normalization leads in the limit of particle-conserving scattering processes and vanishing work function (metal) or electron affinity (semiconductor) to an energy and angle independent unitary emission yield. Although in reality not realizable, this cannot be correct. In the following, we therefore abandon the conditional probability construction and identify the backscattering function $B(E, \eta|E', \eta')$ directly with the function $Q(E, \eta|E', \eta')$, that is, we set

$$B(E, \eta|E', \eta') = Q(E, \eta|E', \eta') \quad (5)$$

with $Q(E, \eta|E', \eta')$ obtained, as before^{27,28,32,33}, from the invariant embedding principle²⁴⁻²⁶.

In its basic form, given by Dashen²⁴ and illustrated in Fig. 2, the principle states that adding an infinitesimally thin layer of the same material on top of a halfspace filled with it does not change the backscattering. Symmetrizing the backscattering function,

$$Q(E, \eta|E', \eta') \rightarrow \sqrt{\rho(E)} Q(E, \eta|E', \eta') \sqrt{\rho(E')}, \quad (6)$$

the principle leads to the embedding equation,

$$G^- + (G^+ - S) \circ Q + Q \circ (G^+ - S) + Q \circ G^- \circ Q = 0, \quad (7)$$

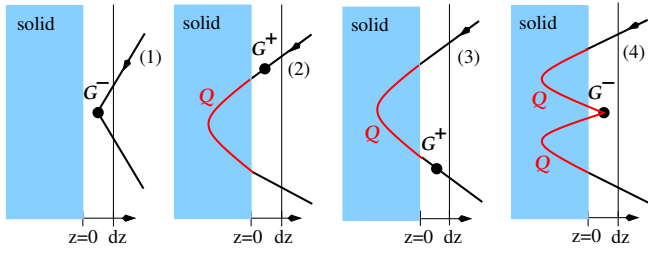


Figure 2. (Color online) Illustration (adopted from Ref.³²) of the embedding principle leading to the nonlinear integral equation (7). Due to the scattering in the infinitesimally thin layer on top of the halfspace filled with the solid, an electron hitting the interface has four additional pathways (1)–(4) available. However, the four paths should not change the backscattering function $Q(E, \eta|E', \eta')$. Hence, the increase in backscattering the four paths induce must cancel with the decrease of backscattering due to the old paths, which is the original $Q(E, \eta|E', \eta')$ multiplied with the probability that scattering occurs at all on the inward and outward bound legs of the path through the layer²⁴.

where the \circ operation is defined by

$$(A \circ B)(E, \eta|E', \eta') = \int_{E'}^E \int_0^1 dE'' d\eta'' A(E, \eta|E'', \eta'') B(E'', \eta''|E', \eta'). \quad (8)$$

The kernels, inverse scattering lengths weighted by the direction of propagation, can be obtained from the Golden Rule transition rates $W^\pm(E, \eta|E', \eta')$ for forward (+) and backward (–) scattering,

$$G^\pm(E, \eta|E', \eta') = \sqrt{\rho(E)} \frac{W^\pm(E, \eta|E', \eta')}{v(E)\eta} \sqrt{\rho(E')}, \quad (9)$$

whereas

$$S(E, \eta|E', \eta') = \frac{\Gamma(E)}{v(E)\eta} \delta(E - E') \delta(\eta - \eta') \quad (10)$$

with

$$\Gamma(E) = \int_{-\chi}^E dE' \int_0^1 d\eta' \rho(E') \left[W^+(E, \eta|E', \eta') + W^-(E, \eta|E', \eta') \right], \quad (11)$$

the total scattering rate at energy E which in fact is independent of η . The transition rates W^\pm will be specified in the next subsection. The numerical strategy to solve the embedding equation (7) follows Shimizu and coworkers^{30,31} who used the invariant embedding approach to study the shielding of γ -rays in nuclear reactors. It is sketched in Appendix A and solves the equation without approximation except the discretization of the integrals.

	Z	$a[\text{\AA}]$	$\chi[\text{eV}]$	$E_g[\text{eV}]$	$\omega_{\text{LO}}[\text{eV}]$	$D_t K [10^8 \frac{\text{eV}}{\text{cm}}]$	ε
Si	4	5.43	4.05	1.11	0.063	11	11.7
Ge	4	5.66	4.0	0.66	0.037	9.5	16.2
	a_1	a_2	a_3	a_4	$E_g^{\text{ave}}[\text{eV}]$	$\rho[\text{g}/\text{cm}^3]$	n_{ion}
Si	-0.992	0.791	-0.352	-0.018	4.8	2.33	0.0073
Ge	-0.955	0.803	-0.312	-0.019	4.2	5.32	0.0065

Table I. Valence Z , lattice constant a , electron affinity χ , energy gap E_g , phonon energy ω_{LO} , optical deformation potential $D_t K$, dielectric constant ε , pseudopotential parameters^{43,44} a_i , average optical energy gap^{40,42} E_g^{ave} , mass density ρ , and atomic density n_{ion} . If not noted otherwise, the material parameters are from Jacoboni and Reggiani⁵⁰ and given in atomic units, with energy measured in Rydbergs, length in Bohr radii, and mass in bare electron masses.

C. Radium-jellium model

In the previous subsection we described a general scheme for the construction of the surface scattering kernel $R(E, \xi|E', \xi')$. To compute numerical values, we have to furnish the approach with a microscopic model for the solid, that is, we have to specify the electronic structure, the interface potential, and the scattering processes inside the semiconductor.

Inspired by the work of Bauer and coworkers^{38,39} we employ for that purpose a radium-jellium-type model, with ion cores randomly immersed in an electron liquid. The elastic scattering of electrons on the ion cores is assumed to be incoherent and described by a screened pseudopotential which is also used in electronic band structure calculations^{43–45}. Screening is subtle in covalently bound solids. We account for it phenomenologically along the lines of Penn⁴², augmented by ideas of Phillips⁴¹ and parameters of Srinivasan⁴⁰. In addition to the scattering on the ion cores, we consider electron-phonon scattering, and as the main energy loss process, impact ionization across the energy gap. The latter causes also electron multiplication and is thus of central importance for secondary electron emission.

The full band structure of the solid cannot be represented by the radium-jellium model. We hence approximate the electronic structure of the semiconductor by a parabolic conduction and a parabolic valence band, separated by a direct energy gap E_g , and both with effective mass equal to the bare electron mass. Taking then an image-step⁴⁶ with depth χ as an interface potential, as indicated in Fig. 1c, the probability for an electron to be quantum-mechanically reflected from the interface region reads⁵¹

$$R(E, \xi) = \left| \frac{\sqrt{\tilde{E}_z} - \sqrt{E_z y}}{\sqrt{\tilde{E}_z} + \sqrt{E_z y^*}} \right|^2 \quad (12)$$

with $E_z = E\xi^2$, $\tilde{E}_z = E_z + \chi$, and

$$y = -2 \frac{W'_{\lambda,1/2}(\xi_0)}{W_{\lambda,1/2}(\xi_0)}, \quad (13)$$

where $W_{\lambda,1/2}(x)$ is a Whittaker function, $W'_{\lambda,1/2}(x)$ its derivative with respect to its argument,

$$\lambda = -i \frac{\varepsilon - 1}{\varepsilon + 1} \frac{1}{\sqrt{8E_z}}, \quad (14)$$

$$\xi_0 = i \frac{\sqrt{2}}{\chi} \frac{\varepsilon - 1}{\varepsilon + 1} \sqrt{E_z}, \quad (15)$$

y^* is the complex conjugate of y , and ε is the dielectric constant of the solid. As in the work for metals²⁸, energy gaps in the reflection probability could be included. But the experimental data for the emission yield of silicon and germanium^{47,48}, the materials we use as an illustration of our approach, do not indicate that this is required.

We are now turning to the scattering processes inside the solid. Measured from the conduction band minimum, electron emission and reflection take place at energies much larger than phonon energies, even the energy of the longitudinal optical phonon $\omega_{LO} \ll E$. It is thus appropriate to describe electron-phonon scattering quasi-elastically and to combine it with electron-ion-core scattering to a single elastic scattering process. Since the latter should be absent at low energies, close to the band minimum, we adopt an idea of Kieft and Bosch⁵² and switch between the two elastic scattering processes. Instead of a smooth crossover we implement however a hard energy threshold E_{th} , above which electrons scatter on the ion cores, whereas below it electrons scatter with phonons. The threshold is the energy, where the electron's de Broglie wave length measured from the bottom of the conduction band is equal to the lattice spacing. Hence, $E_{th} = (2\pi/a)^2 - \chi$ with a the lattice constant and χ the electron affinity. Albeit ad-hoc, it seems plausible to assume that electrons with small wave length do not notice the lattice periodicity, especially when they propagate in arbitrary directions. Indeed, at energies above 100 eV neglecting the periodicity of the lattice potential seems to be generally accepted (but see the recent discussion by Werner⁵³). Systematic work, based on quantum-kinetic equations, which so far has been only done for high energies⁵⁴, is however required to ultimately clarify this point.

The starting point for the calculation of the elastic transition rates is the standard Golden Rule expression. Introducing spherical coordinates in momentum space, with the z -axis pointing along the inward interface normal, states with $k_z > 0$ describe electrons moving inwards the solid, whereas states with $k_z < 0$ denote states moving outwards. It is then straightforward to work out the rates for forward (+) and backward (-) scattering and to express them in terms of the variables defined in Fig. 1b: the total energy E , the direction cosine η , and the azimuth angle Φ , which for a laterally homogeneous

interface does however not appear because it is integrated out. As a result, one obtains

$$W_{\text{elastic}}^{\pm}(E, \eta|E', \eta') = W_{\text{ep}}^{\pm}(E, \eta|E', \eta')\Theta(E_{th} - E) + W_{\text{eic}}^{\pm}(E, \eta|E', \eta')\Theta(E - E_{th}) \quad (16)$$

with $\Theta(x)$ the Heaviside step function,

$$W_{\text{ep}}^{\pm}(E, \eta|E', \eta') = \frac{M^2}{(2\pi)^2} [1 + 2n_B(\omega_{LO})]\delta(E - E') \quad (17)$$

the rate for electron-(longitudinal optical) phonon scattering, where $M^2 = (D_t K)^2 / (\omega_{LO} \rho)$ is the scattering strength and $n_B(\omega) = 1/(\exp(\beta\omega) - 1)$ the Bose function, and

$$W_{\text{eic}}^{\pm}(E, \eta|E', \eta') = \frac{1}{(2\pi)^2 n_{\text{ion}}} \langle |U_{\text{ps}}(g^{\pm})|^2 \rangle_{\Phi} \delta(E - E') \quad (18)$$

the electron-ion-core scattering rate with $\langle \dots \rangle_{\Phi} = \int_0^{2\pi} (\dots) d\Phi$ denoting the integral over the azimuth angle, n_{ion} the atomic density of the solid, and

$$U_{\text{ps}}(q) = \frac{Z/\bar{\varepsilon}}{q^2 + k_s^2} a_1 (\cos(a_2 q) + a_3) \exp(a_4 q^4) \quad (19)$$

the Fourier transform of the pseudopotential⁴³⁻⁴⁵ of an ion with valence Z , phenomenologically screened⁴⁰⁻⁴² as explained below. Its normalization leads to the factor $1/n_{\text{ion}}$ in the scattering rate. Finally,

$$g^{\pm} = |\vec{k} - \vec{k}'|^{\pm} = g(E, T, p = 1|E', T', p' = \pm 1; \Phi), \quad (20)$$

where the function $g(E, T, p|E', T', p'; \Phi)$ is defined in (B20) and $T = (E + \chi)(1 - \eta^2)$ and $T' = (E' + \chi)(1 - (\eta')^2)$ are the lateral kinetic energies of the initial and final state. The material parameters entering the rates are named and listed in Table I.

For energies above the band gap, impact ionization is possible and becomes the main inelastic scattering process. To derive its rate, we switch to the hole representation for the valence band and start with the standard Golden Rule representation as given, for instance, by Kane³⁴. Using spherical coordinates in momentum space with the z -axis pointing again inwards, identifying scattering between states for forward and backward moving electrons, and employing the total energy E , the lateral kinetic energy T (instead of the direction cosine η), and the azimuth angle Φ as independent variables, we obtain

$$W_{\text{impact}}^{\pm}(E, \eta|E', \eta') = \mathcal{W}(E, T, 1|E', T', \pm 1) \quad (21)$$

with the function $\mathcal{W}(E, T, p|E', T', p')$ derived in Appendix B and T and T' the lateral kinetic energies given above.

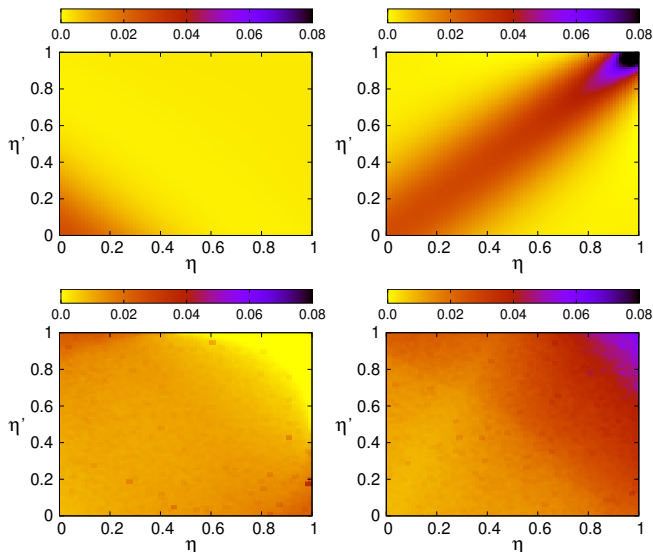


Figure 3. (Color online) Angle dependence of the transition rates for Si using the model described in II C. Left and right panels display for initial energy $E = 28.8$ eV and, from top to bottom, final energies $E' = 28.8$ eV and 1.8 eV the rates $W^-(E, \eta|E', \eta')$ and $W^+(E, \eta|E', \eta')$ as employed for the calculation of $\Gamma(E)$, that is, without the factor two in front of $W_{\text{impact}}^\pm(E, \eta|E', \eta')$. The noise of the Monte Carlo integration required for the computation of the impact ionization transition rate is clearly seen in the lower two panels.

As illustrated in Fig 1c, impact ionization leads to two conduction band electrons^{34–37}. To implement in our formalism the correct ionization rate, we thus have to avoid double counting by correctly normalizing, respectively, the contribution of impact ionization to the kernels $G^\pm(E, \eta|E', \eta')$ and the total scattering rate $\Gamma(E)$. Following the reasoning of Penn and coworkers⁵⁵, as well as Wolff's⁵⁶, we find $W_{\text{impact}}^\pm(E, \eta|E', \eta')$ to be multiplied by a factor two if used in (9) for the kernels $G^\pm(E, \eta|E', \eta')$, whereas the plain $W_{\text{impact}}^\pm(E, \eta|E', \eta')$ enters (11) for the total scattering rate $\Gamma(E)$. Hence, in total, the transition rates to be used in the kernels $G^\pm(E, \eta|E', \eta')$ read $W^\pm(E, \eta|E', \eta') = W_{\text{elastic}}^\pm(E, \eta|E', \eta') + 2W_{\text{impact}}^\pm(E, \eta|E', \eta')$, while in the total scattering rate $\Gamma(E)$ the rates $W^\pm(E, \eta|E', \eta') = W_{\text{elastic}}^\pm(E, \eta|E', \eta') + W_{\text{impact}}^\pm(E, \eta|E', \eta')$ have to be inserted.

In order to complete the model description, the screening of the electric potentials inside the semiconductor has to be specified. Avoiding a selfconsistent calculation of the potentials, we adopt a phenomenological screening model which combines metal- and semiconductor-type screening. Following Phillips⁴¹, we split for that purpose the valence charge into an atomic part, localized close to the ion cores, and a bond part, localized in the bonds between neighboring ions. Anticipating a static dielectric constant ε , denoting by Z the valence of the atoms constituting the solid, and measuring charge in units of the elementary charge e , the bond charge per ion is Z/ε ,

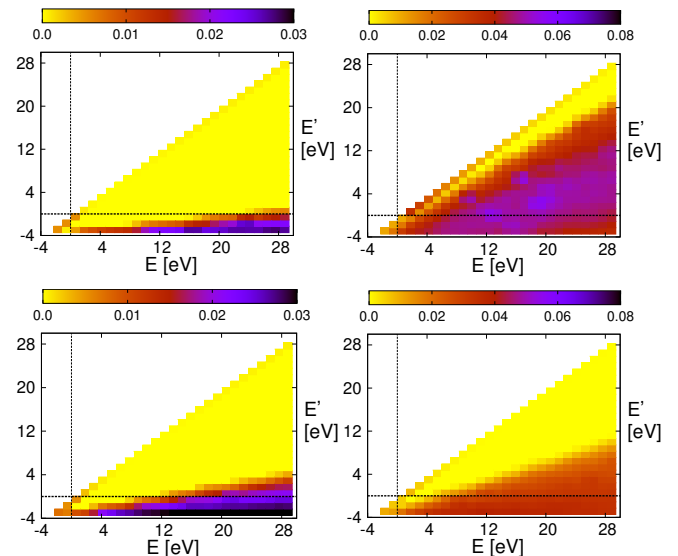


Figure 4. (Color online) Energy dependence of the transition rates for Si using the model described in II C. Left and right panels display $W^-(E, \eta|E', \eta')$ and $W^+(E, \eta|E', \eta')$ as employed for the calculation of $\Gamma(E)$, that is, without the factor two in front of $W_{\text{impact}}^\pm(E, \eta|E', \eta')$ for $\eta = 1$ and, from top to bottom, $\eta' = 0.75$ and 0.24. The dashed lines indicate the just-outside potential energy, which is set to zero.

while the atomic charge per ion is $Z(1 - 1/\varepsilon)$. Assuming now, the atomic charges to perfectly screen the charge of the ions, each ion core carries effectively only a charge Z/ε . Since the bond charge is less localized than the atomic charge, it may approximately give rise to metallic screening, described by a Thomas-Fermi screening wave number k_s defined by

$$k_s^2 = \frac{12\pi n_b}{E_{F,b}} \quad (22)$$

where $n_b = Zn_{\text{ion}}/\varepsilon$ and $E_{F,b} = (3\pi^2 n_b)^{2/3}$ is the Fermi energy associated with the bond part of the valence charge density.

The screened Coulomb part of the ion's pseudopotential would thus become $(Z/\varepsilon)/(q^2 + k_s^2)$ with k_s given by (22). We have to correct however ε for the fact that part of the valence charge is put into metallic screening. This can be done by using Penn's formula⁴² for the dielectric constant of a semiconductor not for the total valence charge but only for the atomic part. Hence, Z in the Coulomb part of the pseudopotential is not multiplied by $1/\varepsilon$ but by $1/\bar{\varepsilon}$ with

$$\bar{\varepsilon} = 1 + \frac{16\pi n_s}{(E_g^{\text{ave}})^2} \left(1 - \frac{E_g^{\text{ave}}}{4E_{F,s}} \right), \quad (23)$$

where $n_s = Zn_{\text{ion}}(1 - 1/\varepsilon)$, $E_{F,s} = (3\pi^2 n_s)^{2/3}$, and E_g^{ave} is the average optical band gap^{41,42}. Put together, we then obtain the screened Coulomb part of the pseudopotential, $(Z/\bar{\varepsilon})/(q^2 + k_s^2)$, as it features in (19).

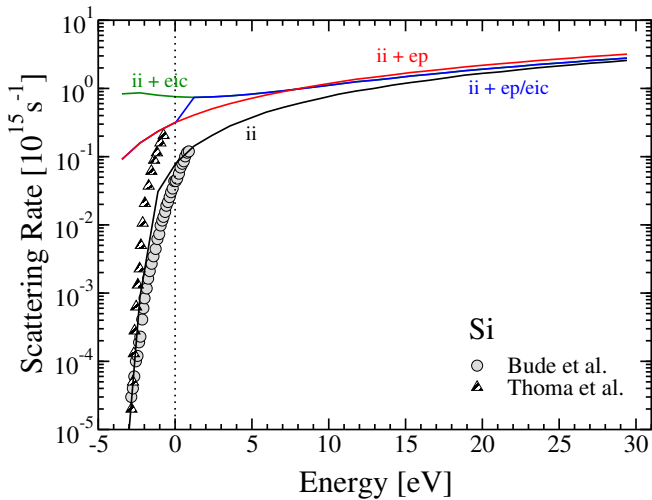


Figure 5. (Color online) Total scattering rate $\Gamma(E)$ defined in (11) for silicon using the material parameters of Table I. For impact ionization alone (ii), $\Gamma(E)$ is in reasonable agreement with results obtained by Bude³⁶ and Thoma³⁵ et al. (as extracted from Fig. 1 of Cartier and coworkers³⁷). Adding on top of it also electron-phonon (ii+ep), electron-ion-core (ii+eip), or both (ii+ep/eic), with the adhoc switching between the two discussed in IIC and visible by the step of the blue line close to the just-outside potential energy, $\Gamma(E)$ changes as shown.

Since the impact ionization rate contains the Coulomb interaction between two electrons, and not between an electron and an ion core, we screen it by the full valence charge density in a metallic manner (see Appendix B). Although this is also an approximation, in spirit, it is consistent with previous calculations of the impact ionization rate in semiconductors^{34–37}.

III. RESULTS

Having established a model for the semiconducting interface, from which the transition rates $W^\pm(E, \eta|E', \eta')$ follow, the kernels of the embedding equation are given and we can solve (7) by the numerical strategy explained in Appendix A to obtain—at the end—the surface scattering kernel $R(E, \xi|E', \xi')$ as well as the emission yield $Y(E, \xi)$. To demonstrate the feasibility of our approach we consider silicon and germanium. The parameters of the model are given in Table I and the temperature of the solid is 300 K. We are particularly interested in low electron impact energies. Setting $E_{\max} = 30$ eV gives a width $\Delta E \simeq 1.2$ eV for the $N = 30$ energy windows into which we split in the numerical implementation the whole energy range from $-\chi$ to E_{\max} . The $M = 80$ discretization steps of the integrals over the direction cosines lead to $\Delta\eta \simeq 0.0127$.

Let us start with numerical data for $W^\pm(E, \eta|E', \eta') = W_{\text{elastic}}^\pm(E, \eta|E', \eta') + W_{\text{impact}}^\pm(E, \eta|E', \eta')$, the transition rates to be used in (11) for the calculation of the total

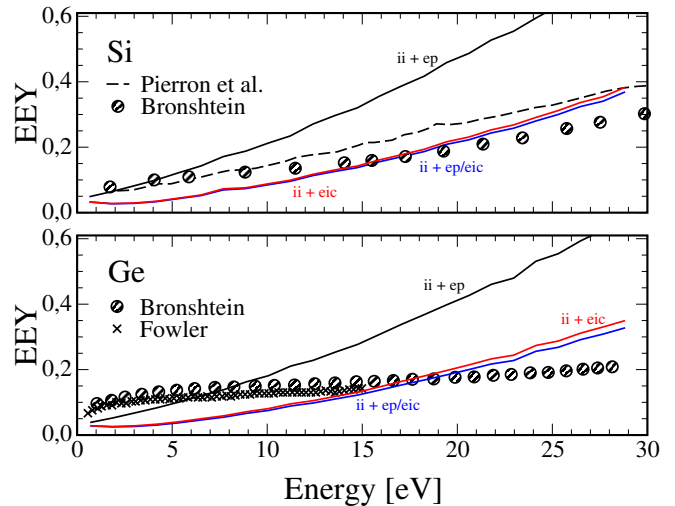


Figure 6. (Color online) Secondary electron emission yield $Y(E, \xi)$ for a silicon and germanium surface after it was hit perpendicularly ($\xi = 1$) by an electron with energy E . Experimental data are from Bronshtein and Fraiman⁴⁸ as well as Fowler and Farnsworth⁴⁷. Monte Carlo data are from Pierron and coworkers⁴⁹. Theoretical results are shown for different scattering processes included into the surface model: impact ionization only (ii), impact ionization and electron-phonon scattering throughout the whole energy range (ii+ep), impact ionization and scattering on ion cores throughout the whole energy range (ii+eic), and impact ionization and scattering on phonons/ion cores below/above $E_{\text{th}} \simeq 1$ eV, as discussed in the main text (ii+ep/eic).

scattering rate $\Gamma(E)$. The rates employed in (9) for the kernels $G^\pm(E, \eta|E', \eta')$ are the same except of the factor two in front of $W_{\text{impact}}^\pm(E, \eta|E', \eta')$ (see discussion in the paragraph after Eq. (21) of the previous section).

The angle dependence of $W^\pm(E, \eta|E', \eta')$ is depicted in Fig. 3 for the energy doublets $(E, E') = (28.8 \text{ eV}, 28.8 \text{ eV})$, representing elastic scattering, and $(28.8 \text{ eV}, 1.8 \text{ eV})$, standing for inelastic scattering. For the chosen initial (E) and final state energies (E'), which are both above the threshold energy $E_{\text{th}} = (2\pi/a)^2 - \chi \simeq 1$ eV, elastic scattering is due to the ion cores. Due to the momentum dependence of the ion's pseudopotentials forward scattering is thus favored. Hence, $W_{\text{impact}}^+(E, \eta|E', \eta')$, shown in the upper right panel, is peaked around $\eta' = \eta$ and $W_{\text{impact}}^-(E, \eta|E', \eta')$, plotted on the upper left, is large only for small η and η' , that is, for grazing scattering events. For initial and final state energies below E_{th} (not shown), where in our model elastic scattering is due to phonons, both rates are isotropic because of the nonpolarity of the phonons, making the scattering strength M^2 in (17) momentum independent. This energy range influences however the surface scattering kernel only indirectly via the total scattering rate $\Gamma(E)$ defined in (11), where the energy integral runs from $-\chi$ to E . Inelastic scattering in our model is due to impact ionization. From the panels of the second row of

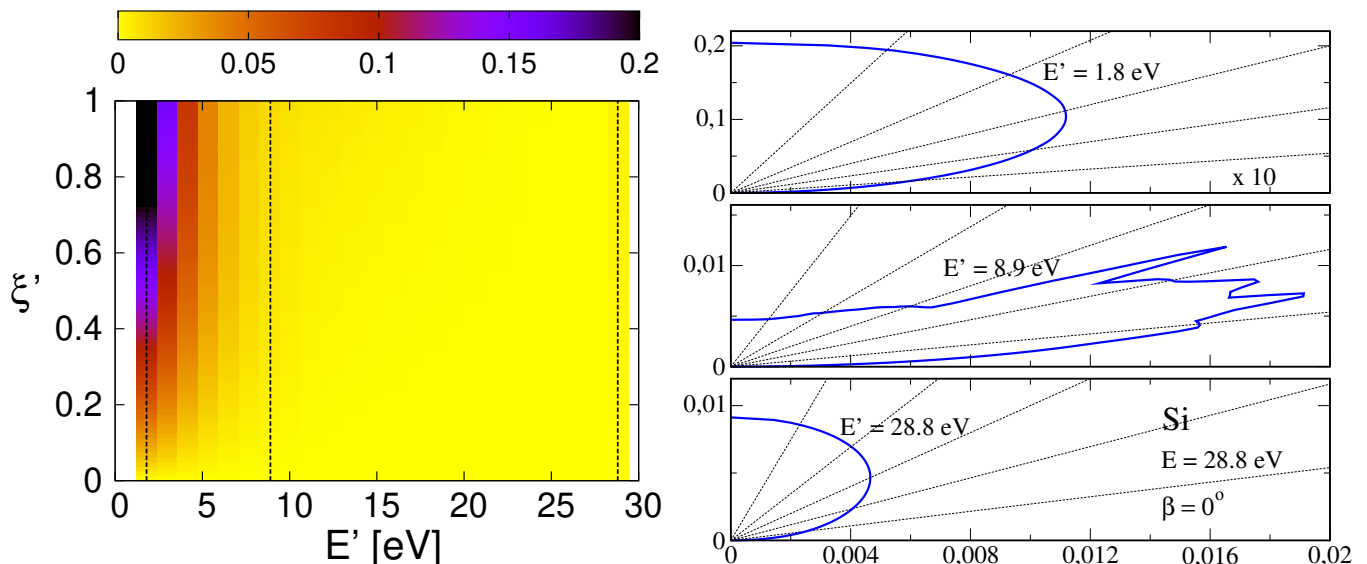


Figure 7. (Color online) Left: Surface scattering kernel $R(E, \xi|E', \xi')$ for Si after a primary electron hit the surface perpendicularly ($\xi = 1$) with $E = 28.8$ eV. Right: Polar representation of the scattering kernel shown on the left for the three final state energies indicated by the vertical dashed lines: $E' = 28.8, 8.9,$ and 1.8 eV. The rays indicate directions in steps of $\Delta\beta' = \pi/12$. Notice the change of scales in the two axes of the upper panel showing the data for $E' = 1.8$ eV. The spikes in the data for $E' = 8.9$ eV are of no physical relevance. They are due to the noise of the Monte Carlo integration (required for the calculation of the impact ionization transition rate) which is particularly strong for final state energies, where $R(E, \xi|E', \xi')$ is rather small.

Fig. 3 it can be inferred that it does not favor any particular forward or backward direction. It is however again strongest in forward direction and there particularly for η and η' close to unity.

Figure 4 depicts the energy dependence of the transition rates for the direction cosine doublets $(\eta, \eta') = (1, 0.75)$ and $(1, 0.24)$. Elastic scattering, below $E_{\text{th}} \simeq 1$ eV due to phonons and above it due to ion cores, is visible along the energy diagonal, whereas impact ionization leads to the off-diagonal data. Of particular relevance for the surface scattering kernel $R(E, \xi|E', \xi')$, and hence also for the secondary emission yield $Y(E, \xi)$, is the fact that impact ionization favors in backward direction for fixed initial and final direction cosines η and η' large energy transfers. Hence, irrespective of the particular choice of η and η' , the rate $W^-(E, \eta|E', \eta')$ is strongest for small E' . In forward direction small energy transfers also occur, leading to $W^+(E, \eta|E', \eta')$ covering larger parts of the EE' plane for a fixed pair η and η' . However, the surface scattering kernel, as well as the emission yield, are determined by the interplay between forward and backward scattering. From the energy dependence of the transition rates $W^\pm(E, \eta|E', \eta')$ we thus expect that most of the backscattered and emitted electrons will have small energy. Hence, they will appear close to the just-outside potential energy indicated by the dashed lines.

To validate at least partly the calculated transition rates $W^\pm(E, \eta|E', \eta')$ we show in Fig. 5 the total scattering rate $\Gamma(E)$ for silicon. Without the elastic scattering processes, $\Gamma(E)$ is the ionization rate and can be compared with the results of others. As discussed by Cartier

and coworkers³⁷, there is a substantial spread in the calculated ionization rates. Below the just-outside potential energy, the rates are sensitive to details of the band structure. Since we are interested at energies above it, we do not enter this discussion. To demonstrate that the ionization rate of our model is plausible, we compare it specifically with the rates obtained by Bude and coworkers³⁶ and Thoma and coworkers³⁵. Notice, both groups calculate the rate only up to 3-4 eV above the conduction band minimum, that is, below the just-outside potential energy. For impact ionization alone (ii), our data are sufficiently close to the data of the two groups, indicating that the semiconductor model we set up produces reasonable data. Adding the scattering on phonons below and the scattering on ion cores above the threshold energy (ii+ep/eic) modifies the rate. In particular, the sharp on-set of impact ionization at $E \simeq -\chi + E_g \simeq -3$ eV is whipped out and the rate assumes finite values all the way down to the bottom of the conduction band. More important for the surface scattering kernel is however the increase of $\Gamma(E)$ above the just-outside potential energy which can be also clearly seen. For comparison, we also plot in Fig. 5 the rate for electrons suffering in addition to impact ionization also elastic scattering on phonons (ii+ep) or ions (ii+eic) throughout the whole energy range.

The numerical data for $\Gamma(E)$ suggest that the model presented in IIC is sufficiently close to reality to expect plausible emission yields and surface scattering kernels. Let us first look at the emission yields for which experimental data exist. Figure 6 shows calculated emission

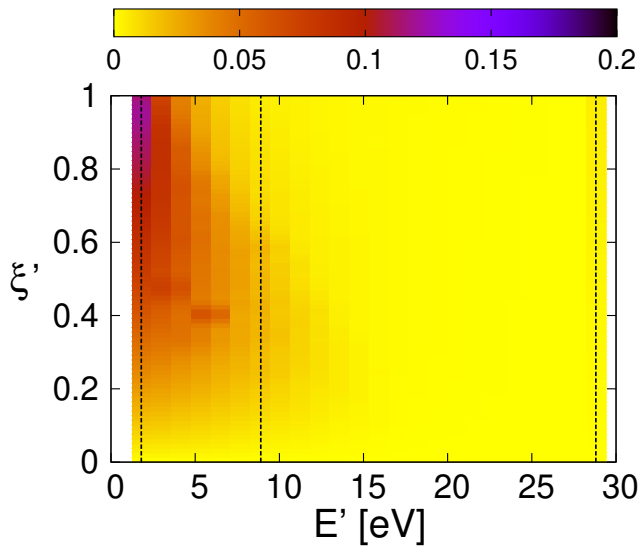


Figure 8. Surface scattering kernel $R(E, \xi|E', \xi')$ for Si after a primary electron hit the surface with energy $E = 28.8$ eV and direction cosine $\xi = 0.37$. The dashed lines indicate the energies for which the ξ' dependence of $R(E, \xi|E', \xi')$ is depicted in Fig. 9

yields for silicon and germanium together with experimental data from Bronshtein and Fraiman⁴⁸, and Fowler and Farnsworth⁴⁷. For silicon the agreement is satisfactory, given the fact that we do not adjust any parameter, working, for instance, with the pseudopotentials also employed in band structure calculations^{43,44}. Our results for silicon are of the same quality as the Monte Carlo results of Pierron and coworkers⁴⁹, who used however a different model. For germanium the discrepancy between calculated and measured yields is larger. Only the order of magnitude is correct. Since silicon and germanium are similar materials, as can be seen from the material parameters, the failure for germanium is surprising. Further measurements as well as calculations are required to clarify the issue. We also plotted again, for comparison, the yields obtained by letting electron-phonon or electron-ion-core scattering act throughout the whole energy range. Due to the isotropy of electron-phonon scattering in nonpolar semiconductors (see Eq. (17)) the yield obtained by impact ionization and electron-phonon scattering (ii+ep) is largest and substantially off the experimental data suggesting that above the just-outside potential energy a different elastic scattering process should prevail. As discussed in IIC scattering on the ion cores should become increasingly important for $E > E_{\text{th}} \simeq 1$ eV. Indeed, combined with impact ionization scattering on ion cores (ii+eic) produces the best results. Since the threshold energy, where we switch between phonon and ion-core scattering is close to the just-outside level, there is hardly any difference to the data (ii+ep/eic) produced by including this switch. The finding is also in accordance with Monte Carlo simulations of secondary electron emission which unisono in-

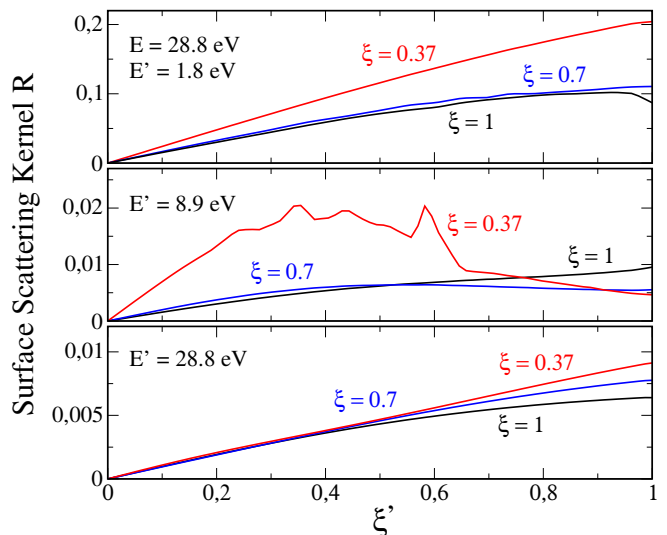


Figure 9. Variation of the surface scattering kernel $R(E, \xi|E', \xi')$ with the direction cosine ξ for $E = 28.8$ eV and $E' = 1.8, 8.9, 28.8$ eV. The peaks in the data for $E' = 8.9$ eV and $\xi = 0.37$ are due to the noise of the Monte Carlo integration required for computing the impact ionization transition rate. They have no physical relevance.

corporate incoherent scattering of electrons on ion cores, as we do, the only difference being in the choice of the scattering potential. Being mostly concerned with energies above 100 eV they employ screened atomic potentials (see, for instance, Pierron et al.⁴⁹, Werner⁵³, and Dapor's book⁵⁷).

Let us finally take a look at representative data for the surface scattering kernel arising from our model for a silicon-plasma interface. Since for germanium the data are similar, we discuss only silicon. Figure 7 depicts on the left $R(E, \xi|E', \xi')$ for initial energy $E = 28.8$ eV and initial direction cosine $\xi = 1$. As expected from the transition rates' favoring of large energy transfers, demonstrated in Fig. 4, the surface scattering kernel is largest close to the just-outside potential energy. The polar plots (in β') of the kernel shown on the right of the figure indicate, moreover, that for perpendicular impact the emission occurs essentially isotropically in all spatial directions compatible with the halfspace geometry. Only electrons emitted at intermediate energies, for instance, $E' = 8.9$ eV show a preferred range of emission directions. However, the magnitude of $R(E, \xi|E', \xi')$ is in this energy range rather small. Hence, the directed emission is rather improbable. The main feature of the data shown on the left of Fig. 7, that the kernel is almost vanishing for $8.9 \text{ eV} < E' < E$, remains intact by reducing E . Only for E of a few eV the separation breaks down.

Of interest is also the dependence of the surface scattering kernel on the direction cosine of impact. Figure 8 plots $R(E, \xi|E', \xi')$ for $E = 28.8$ eV and $\xi = 0.37$, corresponding to $\beta \simeq 46^\circ$. In contrast to the data for $\xi = 1$, that is, for $\beta = 0^\circ$ (perpendicular impact), shown on the

left of Fig. 7, the kernel starts now to reach out for $\xi' < 1$ faintly to larger E' . It seems to be also no longer always largest for $\xi' = 1$.

The dependencies on E' and ξ' can be better read off in Fig. 9, where we plot $R(E, \xi|E', \xi')$ for $E = 28.8$ eV, three impact direction cosines $\xi = 1, 0.7, 0.37$ (corresponding to $\beta = 0, 46^\circ, 68^\circ$), and three emission energies $E' = 28.8, 8.9, 1.8$ eV. The scale of the ordinate of the upper panel, showing the data for $E' = 1.8$ eV, is a factor 10 larger than the corresponding one in the middle and lower panels, indicating that irrespective of the direction of impact $R(E, \xi|E', \xi')$ is in general largest close to the just-outside potential energy. Irrespective of ξ , the magnitude of $R(E, \xi|E', \xi')$ increases moreover for most ξ values monotonously with ξ' . Only at intermediate emission energies $E' \simeq 8.9$ eV and grazing incident, for instance, $\xi = 0.37$, develops $R(E, \xi|E', \xi')$ a very shallow maximum at finite ξ' and hence a preferred range of emission directions away from $\xi' = 1$, as already seen in Fig. 8. The feature occurs, however, in an energy range, where $R(E, \xi|E', \xi')$ is rather small. Most secondary electrons remain hence to be emitted perpendicularly close to the just-outside potential of the surface. Plots for other values of E , ξ , and E' show the same overall features.

To visualize the surface scattering kernel $R(E, \xi|E', \xi')$, a function depending on four continuous variables, in its totality is of course impossible. Many more plots could be produced and put on display. They all look rather similar. For the purpose of demonstrating that the surface scattering kernel $R(E, \xi|E', \xi')$ can be obtained by the invariant embedding approach from a physical model of the plasma-facing solid the plots presented should suffice.

IV. CONCLUSION

We presented a scheme for constructing a boundary condition for the electron energy distribution function of a plasma in contact with a semiconducting solid. Based on the invariant embedding principle for the backscattering function, we derived an expression for the electron surface scattering kernel which takes the electron microphysics inside the solid, responsible for electron backscattering and emission, into account. The kernel connects at the plasma-solid interface the distribution function of the outgoing electrons with the distribution function of the incoming ones. Hence, an electron boundary condition arises which takes material-dependent aspects more faithfully into account as the phenomenological approaches used so far.

As an illustration, we applied the scheme to a silicon and germanium surface, describing the electron's microphysics inside the solids by a radium-jellium model. Approximating the interface potential by an image-step and taking impact ionization as well as incoherent elastic scattering due to phonons and ion cores into account, we deduced from the surface scattering kernel emission

yields in satisfactory agreement with experimental data. For silicon we obtained in fact good agreement, suggesting that the model captures the essential processes leading to electron backscattering and emission sufficiently well.

The main advantage of the embedding approach is that it takes the electron microphysics of the solid into account without tracing the electron distribution function across the plasma-solid interface. It is thus not necessary to run the computation of the surface scattering kernel together with the plasma simulation. The kernel can be computed before hand and stored in a data file. As presented, the approach applies to quasi-stationary situations. It can be, however, generalized to time-dependent situations.

Whereas the transport problem in the form of the embedding equation is completely solved numerically, without linearization and also without an approximate decoupling of direction cosines and energies, the radium-jellium modeling of the electron's microphysics inside the solid may not be the final answer, not only because of the incomplete agreement with experimental data for germanium, but also due to open conceptual issues. In particular, the scattering on the ion cores needs further studies. We assumed the scattering to be completely incoherent, making our model most appropriate for amorphous surfaces. In crystalline solids there should be however also coherent scattering, leading to distinguished directions for backscattering and emission, as well as band gaps above the just-outside potential energy. The mixed screening model, containing semiconductor and metal like elements, needs also further investigations, taking in particular band structure effects into account.

The radium-jellium model is however a good starting point. Provided pseudopotentials for the ion cores are available or can be constructed, it can be applied to other materials as well. Naturally, the scattering and screening processes have to be adjusted case by case, but in its main features, the model applies to semiconductors, dielectrics, as well as metals. The plausibility of the kernels, and hence of the boundary conditions for the electron energy distribution functions, depends on how well the model captures the microscopic processes responsible for electron backscattering and emission. In order to determine the quality of the model, experimental input is critical. Not only measuring the emission yields and backscattering probabilities of freestanding surfaces is required, but also operando surface diagnostics of plasma-exposed surfaces, revealing the structural and chemical state of the surface hit by the electrons of the plasma.

We acknowledge support by the Deutsche Forschungsgemeinschaft through project 495729137.

Appendix A: Numerical approach

The numerical method we adopt for solving the embedding equation (7) is due to Shimizu and coworkers^{30,31}, who used it for studying transport problems in nuclear reactor physics. It utilizes the Volterra-type structure of the energy integrals to transform (7) into a set of matrix equations in the discretized direction cosines and turns out to be surprisingly efficient.

As a first step, the energy space is split into windows of width ΔE and for each function $A(E, \eta|E', \eta')$ a set of functions

$$A_{nm}(\eta|\eta') = \int_n dE \int_m dE' A(E, \eta|E', \eta') f_n(E), \quad (\text{A1})$$

is introduced, where $\int_n dE = \int_{E_n}^{E_{n+1}} dE$ denotes the integration over the n^{th} energy window and $f_n(E) = 1/\Delta E$ is a weight function. In contrast to Shimizu and coworkers, the energy windows we employ have all the same width. Numbering the windows from low to high energy by $n = 1, 2, \dots, N$, and approximating $A(E, \eta|E', \eta') \approx A_{nm}(\eta|\eta') f_m(E')$ for E and E' inside the windows labelled by n and m , respectively, the embedding equation reduces to a set of integral equations in the direction cosines. In a straight manner, one obtains for $m = n$

$$S_n * Q_{nn} + Q_{nn} * S_n = G_{nn}^- + Q_{nn} * G_{nn}^- * Q_{nn} + G_{nn}^+ * Q_{nn} + Q_{nn} * G_{nn}^+ \quad (\text{A2})$$

and for $m < n$

$$S_n * Q_{nm} + Q_{nm} * S_m = K_{nm}^- \quad (\text{A3})$$

with

$$K_{nm}^- = Q_{nn} * G_{nn}^- * Q_{nm} + Q_{nm} * G_{nm}^- * Q_{mm} + G_{nn}^+ * Q_{nm} + Q_{nm} * G_{mm}^+ + G_{nm}^- + D_{nm}^- + C_{nm}^- + A_{nm}^+ + B_{nm}^+, \quad (\text{A4})$$

where we introduced a matrix notation in the direction cosines and the $*$ operation, which is the \circ operation (8) without the energy integration. In addition we defined the matrices

$$A_{nm}^+ = \sum_{l=m}^{n-1} G_{nl}^+ * Q_{lm}, \quad (\text{A5})$$

$$B_{nm}^+ = \sum_{l=m+1}^n Q_{nl} * G_{lm}^+, \quad (\text{A6})$$

$$C_{nm}^- = \sum_{l=m+1}^{n-1} \sum_{p=m}^l Q_{nl} * G_{lp}^- * Q_{pm}, \quad (\text{A7})$$

$$D_{nm}^- = \sum_{p=m}^{n-1} Q_{nn} * G_{np}^- * Q_{pm}. \quad (\text{A8})$$

The crux is now to go through the energy space, that is, through the window indices in such a manner that

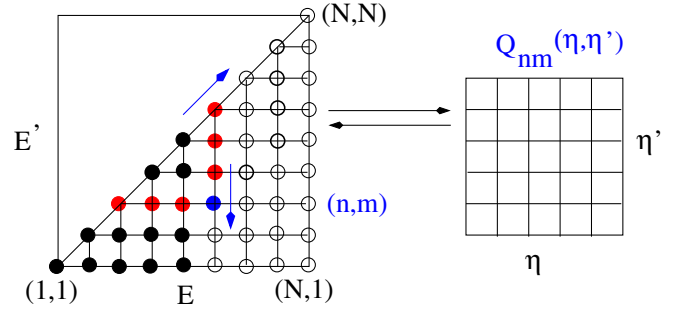


Figure 10. Numerical strategy for solving Eq. (7) for the function $Q(E, \eta|E', \eta')$. Having discretized $Q(E, \eta|E', \eta')$ as described in the text, the algorithm calculates $Q_{nm}(\eta|\eta')$ on an energy grid as indicated, starting with the diagonal $m = n$ and then working its way through $m = n - r$ with $n = 1, 2, \dots, N$ and $r = 1, 2, \dots, n - 1$. Black bullets indicate the grid points for which $Q_{nm}(\eta|\eta')$ is known from the previous steps, whereas open bullets indicate grid points not yet reached. The red bullets are the grid points of the $Q_{lp}(\eta|\eta')$ entering the calculation of $Q_{nm}(\eta|\eta')$ on the actual grid point (n, m) , shown as a blue bullet, by iterating the discretized version of either (A2), if $m = n$, or (A3), if $m < n$, on a grid of discrete direction cosines.

all the matrices $Q_{kr}(\eta|\eta')$ appearing in Eqs. (A5)–(A8) are known from the previous steps of the calculation, enabling thereby an iterative computation of the fixpoints Q_{nn} and Q_{nm} of, respectively, Eq. (A2) and Eq. (A3). As shown in Fig. 10, this is possible by first solving (A2) for the diagonal elements Q_{nn} and then solving (A3) for the off-diagonal elements Q_{nm} with $n > m$, where $m = n - r$ with $n = 1, 2, \dots, N$ and $r = 1, 2, \dots, n - 1$.

In a second step, the integrals over the direction cosine are discretized. Since we have to switch in the expression for the surface scattering kernel (2) from internal (η) to external (ξ) direction cosines, we discretized the η -integrals by a Trapezian rule. Interpolation enables us then to go from η to ξ and vice versa.

At the end, the embedding equation (7) is thus turned into a set of matrix equations. To avoid matrix Riccati and Sylvester equations for Q_{nn} and Q_{nm} , respectively, it is advantageous to leave on the rhs of Eqs. (A2) and (A3) only the diagonal matrices S_n . It is then straightforward to iterate for the fixpoint matrices Q_{nn} and Q_{nm} . For the results discussed in Sect. III we split the energy range $[-\chi, E_{\text{max}}]$ with $E_{\text{max}} = 30$ eV into $N=30$ energy windows and used $M=80$ discretization points for the η -integrals. The function $Q(E, \eta|E', \eta')$, required for the surface scattering kernel, is finally approximated by

$$\rho(E') Q(E, \eta|E', \eta') = \sqrt{\frac{\rho(E')}{\rho(E)}} Q_{nm}(\eta|\eta') f_m(E'), \quad (\text{A9})$$

where E and E' belong to the energy windows n and m , respectively, and the factor involving the density of states arises from the symmetrization (6) which we adopted for a compact representation of the nonlinear term of the embedding equation.

Appendix B: Impact ionization rate

Using spherical coordinates for the electron momenta \vec{k} with the z -axis pointing into the solid and the standard Golden Rule expression^{34–37}, the impact ionization rate due to scattering of a conduction band electron with momentum \vec{k} to one with momentum \vec{k}' becomes, after one internal momentum integration is carried out, energies and lengths are measured in Rydbergs and Bohr radii, and electron and hole masses are set to the bare electron mass,

$$\mathcal{W}(\vec{k}|\vec{k}') = \int d^3q |M(\vec{k}, \vec{k}', \vec{q})|^2 \Psi(E, -\tilde{E}, E', E_{q'}^{\text{CB}}) \quad (\text{B1})$$

with $\vec{q}' = \vec{k} - \vec{k}' + \vec{q}$. The squared matrix element for impact ionization reads in the approximation where overlap integrals between single-electron states are set to unity

$$|M(\vec{k}, \vec{k}', \vec{q})|^2 = 2([U(\vec{k} - \vec{k}')]^2 + [U(\vec{q} - \vec{k}')]^2 - U(\vec{k} - \vec{k}')U(\vec{q} - \vec{k}')) \quad (\text{B2})$$

and the function taking care of the occupancy of the states in the conduction and valence band

$$\Psi(E, -\tilde{E}, E', E_{q'}^{\text{CB}}) = \frac{2}{\pi^3} n_{\text{VB}}(-\tilde{E}) \bar{n}_{\text{CB}}(E_{q'}^{\text{CB}}) \times \delta(E - E' - E_{q'}^{\text{CB}} - \tilde{E}) \quad (\text{B3})$$

with $\bar{n}_{\text{CB}}(E) = 1 - n_{\text{F}}(E + \chi)$ and $n_{\text{VB}}(-\tilde{E}) = 1 - n_{\text{F}}(\tilde{E} - E_g - \chi)$, where $n_{\text{F}}(E) = 1/(\exp(\beta E) + 1)$ is the Fermi function.

In (B3) we anticipated using the total energy E , the lateral kinetic energy $T = (E + \chi)(1 - \eta^2)$ (or, equivalently, the direction cosine η), and the azimuth angle Φ as independent variables for the conduction band states and defined $E = E_k^{\text{CB}} = k^2 + T - \chi$ and $\tilde{E} = -E_q^{\text{VB}} = \tilde{q}^2 + \chi + E_g$, where the minus sign in front of E_q^{VB} signals that \tilde{E} denotes the energy of an hole in the valence band. The electron-electron interaction is given by

$$U(q) = \frac{1}{q^2 + \kappa^2} \quad (\text{B4})$$

with $\kappa^2 = 12\pi n_t / E_{F,t}$ the Thomas-Fermi screening wave number belonging to the total valence charge density $n_t = Zn_{\text{ion}}$ and $E_{F,t} = (3\pi^2 n_t)^{2/3}$ is the Fermi energy associated with it, as discussed at the end of subsection II C.

To proceed, the integration over \vec{q} is transformed into an integration over \tilde{E} , \tilde{T} , and Φ_q , where \tilde{T} is the lateral kinetic energy of the valence band hole. Taking care of the Jacobi determinant associated with this variable transformation, measuring azimuth angles with respect to the projection of \vec{k} onto the xy -plane, which is the interface plane, and using the sign of the z -components of the momenta as labels to distinguish forwardly moving ($p = 1$) from backwardly moving ($p = -1$) electron states, the rate becomes after integrating out \tilde{E} with the help of the energy-conserving δ -function contained in (B3),

$$\mathcal{W}(E, T, p | E', T', p') = \int_0^\infty d\tilde{T} \int_0^{2\pi} d\Phi_{k'} \int_0^{2\pi} d\Phi_q \sum_{i=1}^2 M_i(E, T, p | E', T', p'; \tilde{T}, \Phi_{k'}, \Phi_q) \quad (\text{B5})$$

with

$$M_1(E, T, p | E', T', p'; \tilde{T}, \Phi_{k'}, \Phi_q) = \sum_{\tilde{p}=\pm 1} U(R_1, R_2) N(E, E', \tilde{E}) \frac{\Theta(-c)}{\sqrt{r^2 + 8|c|}} \Big|_{\tilde{q}=\tilde{q}_{\tilde{p}}^{(3)}}, \quad (\text{B6})$$

$$M_2(E, T, p | E', T', p'; \tilde{T}, \Phi_{k'}, \Phi_q) = \sum_{\tilde{p}=\pm 1} \sum_{j=1}^2 U(R_1, R_2) N(E, E', \tilde{E}) \frac{\Theta(c)\Theta(r^2 - 8c)}{\sqrt{r^2 - 8c}} \Big|_{\tilde{q}=\tilde{q}_{\tilde{p}}^{(j)}}, \quad (\text{B7})$$

$$U(R_1, R_2) = 2 \left([U(R_1)]^2 + [U(R_2)]^2 - U(R_1)U(R_2) \right), \quad (\text{B8})$$

$$N(E, E', \tilde{E}) = \pi^{-3} n_{\text{VB}}(-\tilde{E}) \bar{n}_{\text{CB}}(E - E' - \tilde{E}), \quad (\text{B9})$$

and

$$R_1 = |\vec{k} - \vec{k}'|_{pp'} = g(E, T, p | E', T', p'; \Phi_{k'}), \quad (\text{B10})$$

$$R_2 = |\vec{q} - \vec{k}'|_{\tilde{p}p'} = g(\tilde{E}, \tilde{T}, \tilde{p} | E', T', p'; \Phi_q - \Phi_{k'}), \quad (\text{B11})$$

$$\tilde{E} = E_g + \chi + \tilde{T} + \tilde{q}^2, \quad (\text{B12})$$

where $\Theta(x)$ is the Heaviside step function and

$$\tilde{q}_{\tilde{p}}^{(1)} = \frac{|r|}{4} \left(1 + \sqrt{1 - \frac{8c}{r^2}} \right), \quad (\text{B13})$$

$$\tilde{q}_{\tilde{p}}^{(2)} = \frac{|r|}{4} \left(1 - \sqrt{1 - \frac{8c}{r^2}} \right), \quad (\text{B14})$$

$$\tilde{q}_{\tilde{p}}^{(3)} = \frac{|r|}{4} \left(-\tilde{p} \operatorname{sign}(r) + \sqrt{1 + \frac{8|c|}{r^2}} \right). \quad (\text{B15})$$

The functions c and r contained in $M_i(E, T, p|E', T', p'; \tilde{T}, \Phi_{k'}, \Phi_{q'})$ are defined by

$$c(E, T, p|E', T', p'; \tilde{T}, \Phi_q, \Phi_{k'}) = \sqrt{\tilde{T}} h(T, T'; \Phi_q, \Phi_q - \Phi_{k'}) + 2\tilde{T} - E_g - s(E, T, p|E', T', p'; \Phi_{k'}), \quad (\text{B16})$$

$$r(E, T, p|E', T', p') = 2(p\sqrt{E + \chi - T} - p'\sqrt{E' + \chi - T'}), \quad (\text{B17})$$

where

$$h(T, T'; \Phi_q, \Phi_q - \Phi_{k'}) = 2(\sqrt{T} \cos \Phi_q - \sqrt{T'} \cos(\Phi_q - \Phi_{k'})), \quad (\text{B18})$$

$$s(E, T, p|E', T', p'; \Phi_{k'}) = E - E' - [g(E, T, p|E', T', p'; \Phi_{k'})]^2, \quad (\text{B19})$$

$$g(E, T, p|E', T', p'; \Phi_{k'}) = (T + T' - 2\sqrt{TT'} \cos \Phi_{k'} + [p\sqrt{E + \chi - T} - p'\sqrt{E' + \chi - T'}]^2)^{1/2}. \quad (\text{B20})$$

Due to the independent variables E , T , and Φ suggested by the interface geometry, the final expression for the impact ionization rate looks a bit messy. It follows however straight from energy and momentum conservation.

The three remaining integrals in (B5) have to be done numerically. For the data presented in Sect. III we employed the Vegas Monte Carlo integrator of the Numerical Recipes⁵⁸.

-
- ¹ K.-D. Weltmann, J. F. Kolb, M. Holub, D. Uhrlandt, M. Šimek, K. Ostrikov, S. Hamaguchi, U. Cvelbar, M. Černák, B. Locke, et al., *Plasma Process. Polym.* **16**, e1800118 (2019).
- ² R. Michaud and V. Felix and A. Stolz and O. Aubry and P. Lefauchaux and S. Dzikowski and V. Schulz-von der Gathen and L. J. Overzet and R. Dussart, *Plasma Sources Sci. Technol.* **27**, 025005 (2018).
- ³ J. G. Eden, S.-J. Park, J. H. Cho, M. H. Kim, T. J. Houllahan, B. Li, E. S. Kim, T. L. Kim, S. K. Lee, K. S. Kim, et al., *IEEE Trans. Plasma Sci.* **41**, 661 (2013).
- ⁴ R. Dussart, L. J. Overzet, P. Lefauchaux, T. Dufour, M. Kulsreshath, M. A. Mandra, T. Tillocher, O. Aubry, S. Dozias, P. Ranson, et al., *Eur. Phys. J. D* **60**, 601 (2010).
- ⁵ M. D. Campanell, *Phys. Plasmas* **27**, 042511 (2020).
- ⁶ P. Tolias, M. Komm, S. Ratynskaia, and A. Podolnik, *Nucl. Mat. and Energy* **25**, 100818 (2020).
- ⁷ L. Vignitchouk, G. L. Delzanno, P. Tolias, and S. Ratynskaia, *Phys. Plasmas* **25**, 063702 (2018).
- ⁸ P. Tolias, *Plasma Phys. Control. Fusion* **56**, 045003 (2014).
- ⁹ Y. Raitses, D. Staack, M. Keidar, and N. J. Fisch, *Phys. Plasma* **12**, 057104 (2005).
- ¹⁰ A. Dunaevsky, Y. Raitses, and N. J. Fisch, *Phys. Plasma* **10**, 2574 (2003).
- ¹¹ M. M. R. Williams, *Mathematical methods in particle transport theory* (Butterworth, London, 1971).
- ¹² M. N. Kogan, *Rarefied gas dynamics* (Plenum Press, New York, 1969).
- ¹³ Y. L. Al'pert, A. V. Gurevich, and L. P. Pitaevskii, *Space physics with artificial satellites* (Consultants Bureau, New York, 1965).
- ¹⁴ C. Cercignani, *Revista del Nuovo Cimento* **18**, 1 (1995).
- ¹⁵ I. Kuscer, *Surf. Sci.* **25**, 225 (1971).
- ¹⁶ C. Cercignani and M. Lampis, *Transport Theory Stat. Phys.* **1**, 101 (1971).
- ¹⁷ M. M. Becker, G. K. Grubert, and D. Loffhagen, *Eur. Phys. J. Appl. Phys.* **51**, 11001 (2010).
- ¹⁸ D. Loffhagen, F. Sigeneger, and R. Winkler, *J. Phys. D: Appl. Phys.* **35**, 1768 (2002).
- ¹⁹ L. L. Alves, G. Gousset, and C. M. Ferreira, *Phys. Rev. E* **55**, 890 (1997).
- ²⁰ C. Schulze, Z. Donkó, and J. Benedikt, *Plasma Sources Sci. Technol.* **31**, 105017 (2022).
- ²¹ M. Daksha, B. Berger, E. Schuengel, I. Korolov, A. Derzsi, M. Koepke, Z. Donkó, and J. Schulze, *J. Phys. D: Appl. Phys.* **49**, 234001 (2016).
- ²² V. I. Demidov, S. F. Adams, I. D. Kaganovich, M. E. Koepke, and I. P. Kurlyandskaya, *Phys. Plasma* **22**, 104501 (2015).
- ²³ M. Daksha, A. Derzsi, Z. Mujahid, D. Schulenberg, B. Berger, Z. Donkó, and J. Schulze, *Plasma Sources Sci. Technol.* **28**, 034002 (2019).
- ²⁴ R. Dashen, *Phys. Rev.* **134**, A1025 (1964).
- ²⁵ L. G. Glazov and I. Pázsit, *Nucl. Instr. and Meth. B* **256**, 638 (2007).

- ²⁶ M. Azzolini, O. Y. Ridzel, P. S. Kaplya, V. Afanas'ev, N. M. Pugno, S. Taioli, and M. Dapor, *Comp. Mat. Sci.* **173**, 109420 (2020).
- ²⁷ F. X. Bronold and H. Fehske, *Phys. Rev. Lett.* **115**, 225001 (2015).
- ²⁸ F. X. Bronold and H. Fehske, *J. Appl. Phys.* **131**, 113303 (2022).
- ²⁹ P. Cagas, A. Hakim, and B. Srinivasan, *J. Comput. Phys.* **406**, 109215 (2020).
- ³⁰ A. Shimizu and H. Mizuta, *J. Nucl. Sci. Technol.* **3**, 57 (1966).
- ³¹ A. Shimizu and K. Aoki, *Application of invariant embedding to reactor physics* (Academic Press, New York, 1972).
- ³² F. X. Bronold and H. Fehske, *Plasma Phys. Control. Fusion* **59**, 014011 (2017).
- ³³ F. X. Bronold, F. Fehske, M. Pamperin, and E. Thiessen, *Eur. Phys. J. D* **72**, 88 (2018).
- ³⁴ E. O. Kane, *Phys. Rev.* **159**, 624 (1967).
- ³⁵ R. Thoma, H. J. Pfeifer, W. L. Engl, W. Quade, R. Brunetti, and C. Jacoboni, *J. Appl. Phys.* **69**, 2300 (1991).
- ³⁶ J. Bude, K. Hess, and G. J. Iafrate, *Phys. Rev. B* **45**, 10958 (1992).
- ³⁷ E. Cartier, M. V. Fischetti, E. A. Eklund, and F. R. McFeely, *Appl. Phys. Lett.* **62**, 3339 (1993).
- ³⁸ E. Bauer, *J. Vac. Sci. Technol.* **7**, 3 (1970).
- ³⁹ W. Dietzel, G. Meister, and E. Bauer, *Z. Phys. B* **47**, 189 (1982).
- ⁴⁰ G. Srinivasan, *Phys. Rev.* **178**, 1244 (1969).
- ⁴¹ J. C. Phillips, *Phys. Rev.* **166**, 832 (1968).
- ⁴² D. R. Penn, *Phys. Rev.* **128**, 2093 (1962).
- ⁴³ J. Ihm, S. G. Louie, and M. L. Cohen, *Phys. Rev. B* **18**, 4172 (1978).
- ⁴⁴ M. Schlüter, J. R. Chelikowsky, S. G. Louie, and M. L. Cohen, *Phys. Rev. B* **12**, 4200 (1975).
- ⁴⁵ J. C. Phillips, *Bonds and bands in semiconductors* (Academic Press, New York, 1973).
- ⁴⁶ L. A. MacColl, *Phys. Rev.* **56**, 699 (1939).
- ⁴⁷ H. A. Fowler and H. E. Farnsworth, *Phys. Rev.* **111**, 103 (1958).
- ⁴⁸ I. M. Bronshtein and B. C. Fraiman, *Secondary electron emission* (Nauka, Moscow, 1969).
- ⁴⁹ J. Pierron, C. Inguibert, M. Belhaj, T. Gineste, J. Puech, and M. Raine, *J. Appl. Phys.* **121**, 215107 (2017).
- ⁵⁰ C. Jacoboni and L. Reggiani, *Rev. Mod. Phys.* **55**, 645 (1983).
- ⁵¹ K. Rasek, F. X. Bronold, and H. Fehske, *Phys. Rev. E* **105**, 045202 (2022).
- ⁵² E. Kieft and E. Bosch, *J. Phys. D: Appl. Phys.* **41**, 215310 (2008).
- ⁵³ W. W. Werner, *Front. Mater.* **10**:1202456 (2023).
- ⁵⁴ S. L. Dudarev, L.-M. Peng, and M. J. Whelan, *Phys. Rev. B* **48**, 13408 (1993).
- ⁵⁵ D. R. Penn, S. P. Apell, and S. M. Girvin, *Phys. Rev. B* **32**, 7753 (1985).
- ⁵⁶ P. A. Wolff, *Phys. Rev.* **95**, 56 (1954).
- ⁵⁷ M. Dapor, *Transport of energetic electrons in solids* (Springer Nature, Cham, Switzerland, 2020).
- ⁵⁸ W. H. Press, S. A. Teukolsky, W. T. Vetterling, and B. P. Flannery, *Numerical recipes* (Cambridge University Press, Cambridge, 1996).